This is the author's version of an article that has been published in this journal. Changes were made to this version by the publisher prior to publication.
The final version of the record is available with Digital Object Identifier 10.1109/TMTT.2020.3006869

Frequency and Bandwidth Tunable Mm-Wave Hairpin Band-Pass Filters using Microfluidic Reconfiguration with Integrated Actuation

Enrique González, *Student Member, IEEE* and Gokhan Mumcu, *Senior Member, IEEE*

Abstract— **Microfluidically reconfigurable radio frequency (RF) devices in general have been found attractive for low-loss, wide frequency tunability and high-power handling capabilities. Recently, integrated actuation of microfluidically reconfigurable devices have been proposed for compact mm-wave device applications. This paper for the first time introduces microfluidically reconfigurable frequency and/or bandwidth tunable band-pass filters (BPFs) operated at mm-wave band with integrated actuation. The BPFs consist of coupled hairpin resonators. Frequency tuning is achieved by capacitively loading the resonators. Bandwidth tuning is achieved by creating varying capacitive loading among the resonators to control the inter-resonator couplings. The capacitive loading mechanisms are realized with selectively metallized plates (SMPs) that can be repositioned within microfluidic channels. The microfluidic channels are located directly above the stationary metallizations of the filter. Piezoelectric bending actuators placed under the filter's ground plane provide the SMP motion capability. The BPFs perform with worst-case insertion loss of 3.1 dB. Frequency tuning capable filters operate within 28 GHz – 38 GHz band. Fractional bandwidth tunability varies from 7.8% to 16.7% at 38 GHz and 7.6% to 12.5% at 28 GHz for the filter that is capable of both tuning mechanisms. The filters are characterized to handle 5 W of continuous RF power without needing thick ground planes or heat sinks. In addition, the frequency tuning speed is characterized to be 285 MHz/ms.**

Index Terms—**microfluidics; band-pass, bandwidth tunability, frequency tunability, mm-wave, reconfigurable filter.**

I. Introduction

MICROFLUIDICALLY reconfigurable RF devices have attracted interest for providing high-power handling capability, high linearity, wide frequency tunability, low-loss, high radiation efficiency, and cost-effective implementations by eliminating active control components such as diodes and varactors [1, 2]. Microfluidically tunable filters [3], antennas [4, 5], antenna arrays [6, 7] and switches [8-11] have been successfully designed and implemented in recent literature to demonstrate a set of these advantages.

Device reconfiguration with microfluidics is primarily achieved with the motion of metallic liquids or metallized solids within microfluidic channels. The channels are often placed within the close proximity of the metallic traces that form the device that is intended to be reconfigured. The metallic liquid or solid within the channel typically is used to implement a varying capacitive loading mechanism. The use of liquid metals within the channels opens the possibility of flexible and self-healing type of reconfigurable device implementations. However, liquid metals exhibit reliability challenges due to oxidization and reduced conductivity drawbacks for mm-wave applications [1, 2]. Utilizing selectively metallized plates (SMPs) within the microfluidic channels alleviates the mm-wave drawbacks of liquid metals. SMP approach has been successfully demonstrated for low-loss performance [12], high-power handling [3, 4] and mm-wave frequency operation [6, 13]. In these previous works, SMPs have been repositioned within the microfluidic channels by employing external micropumps. However, our recent work has demonstrated that SMPs can be repositioned with integrated piezoelectric actuators [11]. This is possible due to the significantly reduced device sizes within the mm-wave frequencies. By carefully designing the channel sizes, small deflections generated by the piezoelectric actuator can be transformed into larger SMP motion. Integrated actuation eliminates the necessity of bulky external micropumps and provides a path for utilizing microfluidics based reconfiguration techniques within the mm-wave frequencies.

The actuation times so far has been shown to be on the order of 1.12 – 3.6 ms [11, 14] for the mm-wave switch realizations. The actuation time can be potentially decreased with material choices, shapes, and design variations. Actuation times on the order of few ms could make the microfluidics based reconfiguration attractive for mm-wave applications that need high power handling, large tuning range, and low loss. Moreover, the low actuation time enables to perform reliability and repeatability tests in the order of millions of cycles [11].

The goal of this manuscript is to demonstrate for the first time the design and realization of microfluidically reconfigurable band pass filters (BPFs) operating in mm-wave bands with frequency and bandwidth tunability capabilities. This is motivated from our earlier work on frequency tunable microfluidic BPFs [3, 12, 15]. These earlier filters required external pumps, operated at lower GHz frequencies and provided only the frequency tuning capability. As mentioned

Manuscript received April 3, 2020; revised June 13, 2020; accepted June 18, 2020. This work was supported in part by the National Science Foundation (NSF) under CAREER Award ECCS-1351557 and NSF Award ECCS-1920926. *(Corresponding author: Gokhan Mumcu.)*

The authors are with the Center for Wireless and Microwave Information Systems (WAMI), Department of Electrical Engineering, University of South Florida, Tampa, FL 33620 USA (e-mail: mumcu@usf.edu).

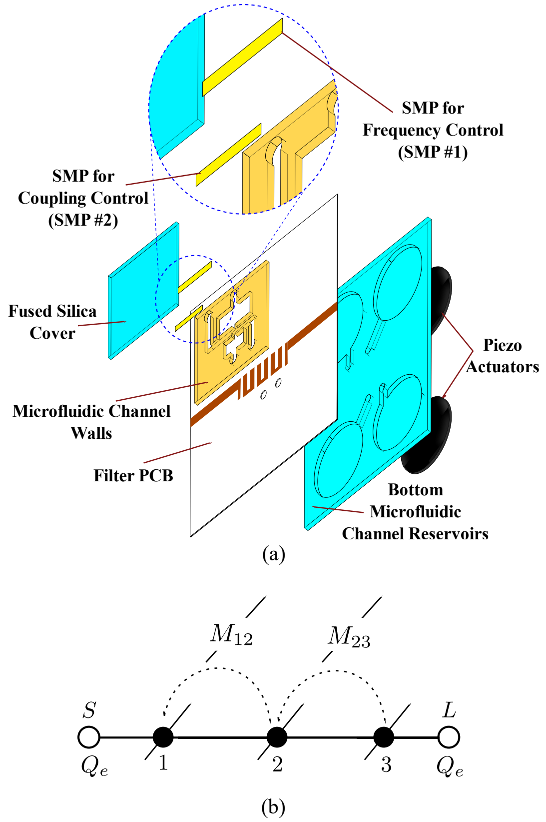

Fig. 1. (a) Substrate stack-up of the frequency and bandwidth tunable filter with integrated actuation; (b) Coupling diagram.

above, their reliability is not well-established in terms of number of cycles the filters could be reconfigured due to the slow time response. In addition, there is no prior work on providing simultaneous reconfiguration capability for bandwidth and frequency (i.e. dual-reconfigurability).

The proposed filter for dual-reconfigurability is shown in Fig. 1(a). Piezoelectric actuators are placed under the ground plane to drive two SMPs in two separate microfluidic channels for providing independent control of frequency and bandwidth. Specifically, this manuscript discusses three separate filter designs and prototypes. The first design is a frequency tunable band pass filter (FT-BPF). The second design is a bandwidth tunable band pass filter (BT-BPF). The third design can be considered as combination of the two filters providing bandwidth and frequency tuning capabilities simultaneously (FBT-BPF). The filter topology is based on a third order coupled resonator BPF where resonance frequencies and inter-resonator couplings must be simultaneously tuned for the desired functionalities [see Fig. 1(b)]. Section II presents the dual-reconfiguration approach with resonator design. Section III presents the FT-BPF design. Frequency tuning range is selected to be 28 GHz – 38 GHz band due to emerging interest in mm-wave communications. The FT-BPF is designed to maintain a constant 7% fractional bandwidth (FBW) within the band. This is motivated from the bandwidth of 28 GHz (e.g. 27 GHz – 29 GHz and 26.5 GHz – 29.5 GHz) and 38 GHz (e.g. 36.5 GHz – 39.5 GHz and 37 GHz – 41 GHz) frequency bands [16, 17]; however, different design specifications can also be pursued. Section IV details the BT-BPF design carried out at 38 GHz. The filter offers 7% to 16% FBW control. Section V presents the FBT-BPF design that operates with frequency tuning range from 28 GHz to 38 GHz while achieving bandwidth tunability from 7% to 12% at 28 GHz and 7% to 16% at 38 GHz. Section VI provides the fabrication details. Section VII details the experimental verification of the filters. Section VIII presents the repeatability and power handling characterization of the filters. It is shown that the filter prototypes perform with worst-case insertion loss (IL) of 3.1 dB at 38 GHz. They offer 7.8%–16.7% 3 dB FBW tunability at 38 GHz and 7.6%–12.5% 3dB FBW tunability at 28 GHz. A reconfiguration speed of 285 MHz/ms is achieved and actuation cycles up to 12 million are demonstrated. The FBT-BPF is characterized to handle up to 5 W of continuous RF power without needing thick ground planes or heat sinks.

II. Frequency and Bandwidth Tuning Principles

The coupling diagram in Fig. 1(b) demonstrates the concept of achieving frequency and bandwidth tunability from a third order BPF. Resonance frequencies of the resonators and their inter-resonator coupling coefficients must be controllable. For a symmetrical filter response, the coupling coefficients M_{12} and M_{23} need to be equal along with synchronized resonance frequencies. External quality factor (Q_e) and coupling coefficients can be determined from the coupled resonator filter theory [18] to achieve the desired filter response and FBW. For well-known filter types (such as Chebyshev and maximally flat), the link between low-pass filter prototype and coupling coefficients is already established [18].

Frequency tunability of microwave filters is commonly achieved by capacitively loading the resonators or modifying the physical dimensions of the resonators. A well-known approach for capacitive loading based frequency tunability is microstrip combline topologies implemented with varactors [19]. A similar capacitive loading approach is demonstrated with microfluidics in [15] where the repositionable SMP metallizations act as the varactors loading the resonators. A well-known approach for physical dimension variation based frequency tunability is the semiconductor [20] or MEMS switch loaded resonators [21]. Physical variation based frequency is tuning is also shown to be possible with microfluidics in [3] where repositionable SMP acts as the resonator itself. Bandwidth tunability of microwave filters is also commonly achieved with capacitive loading to modify the inter-resonator couplings. Simultaneous frequency and bandwidth control increases the number of the control elements (i.e. varactors and/or switches) and penalizes the IL of the filter. This becomes high in mm-wave frequencies with IL values reaching up to 9 dB at 20 GHz (see Table I in Section VIII for comparison of state of the art and presented filters). On the other hand, frequency and/or bandwidth tunable filters have never been implemented in mm-wave frequencies with microfluidics. As will be shown, these filters can offer significant advantages in IL and power handling capability from a compact footprint.

Implementing independent control for frequency and

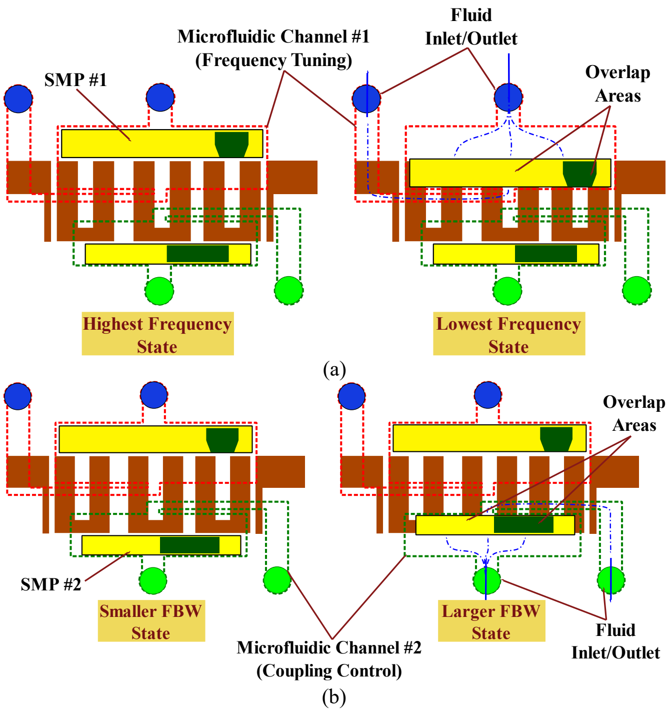

Fig. 2. Filter layouts demonstrating (a) frequency reconfiguration with SMP #1 (SMP #2 is taken to be not loading the filter); (b) bandwidth reconfiguration with SMP #2 (SMP #1 is taken to be not loading the filter).

bandwidth tunability with microfluidics necessitates to utilize two distinct SMPs within two separate microfluidic channels. Therefore, the coupled resonator filter topology consisting of hairpin resonators is proposed as shown in Fig. 1 and Fig. 2. The hairpin resonators allow to use an SMP to simultaneously load the open ends of the resonators for achieving frequency tunability [see Fig. 2(a) SMP #1]. Another SMP can be used at the opposite sides of the hairpin resonators to control inter-resonator couplings through capacitive loading [see Fig. 2(b) SMP #2]. Having SMPs at opposite sides of the resonators allows to realize the filter by making use of meandered microfluidic channels. The channel layout demonstrating this operation is also highlighted with dashed lines in Fig. 2. Each microfluidic channel can be interfaced with a piezoelectric actuator at the back of the ground plane to provide individual control of the SMP positions as shown in 3D perspective view of the filter in Fig. 1. These piezo actuators operate with the same principle and mechanism as introduced in [11].

Fig. 3(a) shows the equivalent circuit of two adjacent resonators loaded with the SMPs. In this circuit model, each hairpin resonator is represented with a parallel L_0C_0 network. These resonators in general exhibit mixed magnetic and electric couplings. However, for the selected geometry and orientation of adjacent resonators, the electrical coupling dominates for small resonator spacing [22] and the performance of the equivalent circuit gets dominated by the electrical coupling capacitance C_m. Within the circuit, coupling is represented with an admittance inverter network. The capacitive loading between the two resonators generated by the metal trace of the SMP #2 is represented with a variable capacitor C_C placed in parallel with the admittance inverter network. The capacitive

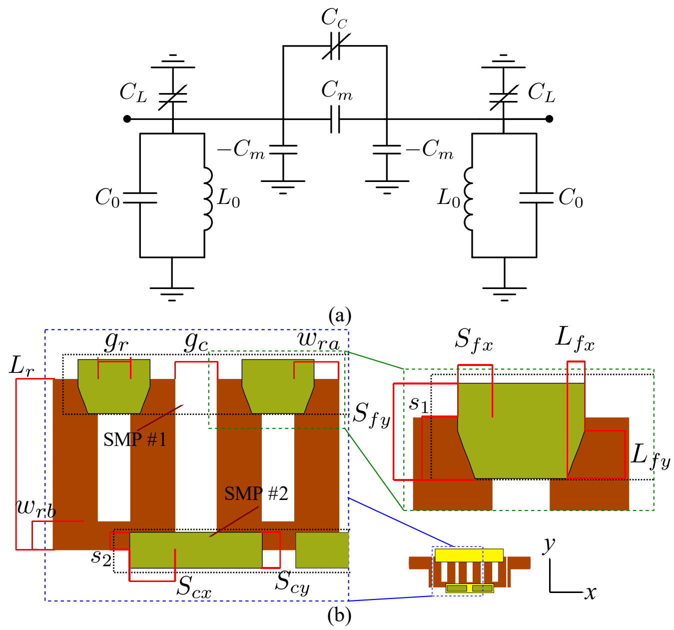

Fig. 3. (a) Equivalent circuit model of a coupled resonator pair and (b) layout detail of the resonator pair when loaded with SMP metallizations ($L_r = 0.95$, $w_{ra} = 0.25$, $w_{rb} = 0.16$, $g_r = 0.18$, $g_c = 0.1$, $S_{fx} = 0.105$, $S_{fy} = 0.3$, $L_{fx} = 0.055$, $L_{fy} = 0.15$, $S_{cx} = 0.25$, $S_{cy} = 0.175$, $0 \geq s_1 \geq S_{fy}$, $0 \geq s_2 \geq S_{cy}$; all units are in mm).

loading introduced by the SMP #1 metal trace across the open ends of the resonator is represented with the variable loading capacitor C_L.

The resonance frequency of the resonator is given by

$$f_0 = \frac{1}{2\pi\sqrt{L_0(C_0 + C_L)}}. \tag{1}$$

Keysight ADS Momentum suite is used for electromagnetics (EM) simulations to design the unloaded resonator operate at 38 GHz. Co-simulation is performed and the C_L value that reduces the resonance frequency down to 28 GHz is identified as 0.3 pF (i.e. 0.3 pF > C_L > 0 for 28 GHz > f_0 > 38 GHz). Co-simulations and equation (1) is utilized at different operation frequencies to extract L_0 and C_0 as 48.314 pH and 0.363 pF, respectively. Afterwards, C_L must be related to the SMP metallizations to realize the filter. For design simplicity, in this work, the C_C and C_L are related to SMP metallizations through the parallel plate capacitor equations. As shown in Fig. 3(b), the metal trace of SMP #1 overlaps with the open ends of the hairpin resonator with an area proportional to $S_{fx} \times S_{fy}$, where S_{fx} and S_{fy} denote the maximum horizontal and vertical overlap lengths of the SMP #1 metallization with respect to the resonator, respectively. Parameter s_1 defines the position of SMP #1 relative to the resonator (e.g. $s_1 = 0$ implies no overlap and $s_1 = S_{fy}$ implies maximum overlap). The shape of the metal traces of SMP #1 is partially trapezoidal to linearize the frequency tuning with respect to s_1 as was similarly employed in [3]. The parameters L_{fx} and L_{fy} shown in Fig. 3(b) describe the shape of the partial trapezoidal area. The relationship between the total overlap area (A_{C_L}) and C_L is

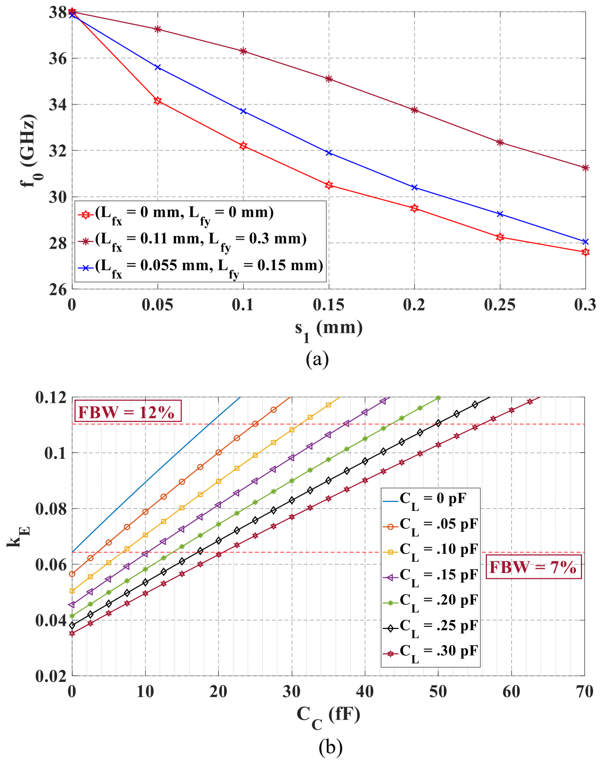

Fig. 4. (a) Resonance frequency variation of the hairpin resonator as a function of SMP #1 position s_1 with different L_{fx} and L_{fy} parameters used in defining the SMP #1 metallization; (b) Coupling as a function of C_L and C_C.

$$C_L = \frac{\varepsilon_r \varepsilon_0 A_{C_L}}{4d}, \tag{2}$$

where d is the vertical separation between the SMP metallizations and printed circuit board (PCB) traces forming the resonators (d = 10 µm); and ε_r is the relative dielectric constant of the material separating the SMP metallizations and PCB traces (ε_r = 2.15). From the described geometry in Fig. 3(b), A_{C_L} is linked to the geometry as

$$A_{C_L} = \begin{cases} 2(S_{fx} - L_{fx})s_1 + \dfrac{L_{fx}s_1^2}{L_{fy}} & \text{for } s_1 < L_{fy} \\ 2S_{fx}s_1 - L_{fx}L_{fy} & \text{for } s_1 \geq L_{fy} \end{cases}. \tag{3}$$

The factor of 4 in equation (2) appears due to the C_L being formed through the series connection of two capacitors defined by the half of the total overlap area. Fig. 4(a) presents the relationship between s_1 and f_0. This relationship is obtained from EM simulations. Frequency variation with s_1 can be linearized by utilizing the L_{fx} and L_{fy} parameters. In the design, S_{fx} is selected as 0.11 mm due to the need to include coupling compensation traces in SMP #1 (see Section III for coupling compensation discussion). With this value of S_{fx}, L_{fx}= 50 µm and L_{fy} = 0.15 mm achieves an almost linear frequency variation behavior with respect to s_1. Subsequently, S_{fy} is determined as 0.3 mm from equations (2) and (3) by making using of the maximum value of C_L = 0.3 pF at $s_1 = S_{fy}$.

To achieve the desired minimal FBW tunability of 9.5% ± 2.5%, the tunability range of C_C must be determined. C_C is proportional to the area $S_{cx} \times S_{cy}$ formed by overlapping metal trace of SMP #2 with the hairpin resonator. Here, S_{cx} and S_{cy} denote the maximum horizontal and vertical overlap lengths of the SMP #2 metallization with respect to the resonator. Parameter s_2 defines the position of SMP #2 with respect to the resonator (e.g. s_2 = 0 implies no overlap and $s_2 = S_{cy}$ implies maximum overlap). The total overlap area A_{C_C} for C_C is rectangular since this shape is found to readily provide a linear coupling variation with s_2. The relationship between A_{C_C} and C_L is

$$C_C = \frac{\varepsilon_r \varepsilon_0 A_{C_C}}{4d}, \tag{4}$$

From the described geometry in Fig. 3(b), A_{C_C} is linked to the geometry as

$$A_{C_C} = 2S_{cx}s_2 \tag{5}$$

From the equivalent circuit of Fig. 3(a), with the approach described in [18], the electrical coupling factor k_E is expressed as:

$$k_E = \frac{f_m^2 - f_e^2}{f_m^2 + f_e^2}, \tag{6}$$

where

$$f_e = \frac{1}{2\pi\sqrt{L_0(C_0 + C_m + C_L + 2C_C)}} \tag{7}$$

$$f_m = \frac{1}{2\pi\sqrt{L_0(C_0 + C_L - C_m)}}. \tag{8}$$

Equations (1) and (6) – (8) show that C_L reduces k_E while also reducing f_0. Therefore, dependence of k_E to C_C must be extracted for different values of C_L as shown in Fig. 4(b). To determine required k_E, a filter topology must be selected. In this manuscript, we pursue a third-order 0.1 dB ripple Chebyshev filter with minimal FBW tunability from 7% to 12%. From [23], low-pass prototype element values can be obtained as $g_0 = g_4 = 1$, $g_1 = g_3 = 1.0316$ and $g_2 = 1.1474$. For FBW of 7%, $Q_e = 14.74$, $M_{12} = M_{23} = 0.06434$. For FBW of 12%, $Q_e = 8.597, M_{12} = M_{23} = 0.1103$. Therefore, k_E needs to be tunable within the range of 0.064 – 0.11. Minimum FBW is achieved when C_C = 0. As described in introduction, a design goal is to maintain minimum FBW as 7% at all possible center frequencies. To achieve this, $C_L = 0$ and C_C = 0 point in Fig. 4(b) is adjusted with the choice of C_m = 23.36 fF to provide the minimum required k_E of 0.064. As seen in Fig. 4(b), for C_L = 0, C_C must be varying from 0 to 20 fF to increase the FBW from 7% to 12%. In the case of C_L = 0.30 pF, C_C needs to vary from 20 fF to 60 fF to tune FBW from 7% to 12%. In the following section, coupling capacitive loading ranging from 0 to 20 fF will be provided with SMP #1 metallizations to ensure a constant FBW filter with minimum of 7% FBW. SMP #2

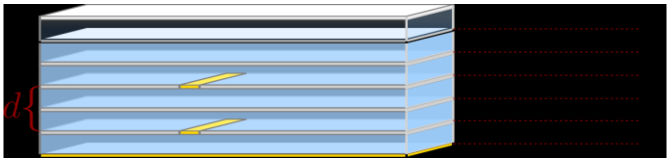

Fig. 5. Substrate stack-up used for Keysight ADS Momentum EM simulations.

metallizations will be designed to provide coupling capacitance tunability ranging from 0 fF to 40 fF. For realizing C_C, S_{cx} is chosen as the resonator arm width w_{ra} = 0.25 mm. and S_{cy} is calculated from (4) and (5) for C_C = 40 fF at $s_2 = S_{cy}$. Fig. 4(b) also demonstrates that k_E depends almost linearly to C_C, thus, justifying the use of rectangular area for coupling capacitors.

Fig. 5 presents the substrate stack-up used to design the filter in Keysight ADS Momentum. A 203 µm Rogers RO4003C substrate (ε_r = 3.55, $\tan\delta$ = 2.7×10^{-3}) with 17.5 µm copper-cladding is used for the PCB hosting the resonators. A 5 µm thick layer is used to represent the liquid between the PCB and SMP metallizations. The liquid is Sigma-Aldrich Fluorinert FC-40 (ε_r = 1.9, $\tan\delta$ = 2×10^{-4}). The thickness of this liquid layer is due to the fabrication tolerances in realizing the height of the microfluidic channels. A 5 µm thick Parylene N (ε_r = 2.4, $\tan\delta$ = 2×10^{-4}) layer is deposited on the SMP metallizations to ensure a dielectric insulation between SMP and the PCB metallizations. A 305 µm thick Rogers RO4003C substrate is selected for the SMP. The channel is sealed with a 500 µm thick fused silica substrate (ε_r = 3.81, $\tan\delta$ = 4×10^{-4}).

Fig. 3(b) shows the physical dimensions of the resonator designed to operate at 38 GHz in its unloaded state within the selected substrate stack-up. Through EM simulations, inter-resonator spacing is determined to be g_c = 0.1 mm to provide the desired k_E. The SMP metallization dimensions determined from the circuit analysis are slightly tuned in ADS simulations to provide the desired frequency and bandwidth tuning. The finalized dimensions of the SMP metallization areas are also provided in Fig. 3(b). The resonator is expected to provide an unloaded quality factor of $Q_u \approx$ 115. The unloaded quality factor will be mainly limited by the technology used for the resonators, followed by the required capacitances (and their inherent dielectric losses) needed to realize frequency and bandwidth reconfiguration. Similar as with active varactor tunable filter applications.

III. Frequency Tunable Filter Design

The design of the resonator is detailed in previous section. Fig. 6(a) shows the layout of the FT-BPF with 7% constant FBW. As detailed in previous section, SMP #1 includes multiple metallization traces for frequency tuning and k_E compensation as the frequency is lowered with s_1 motion of the SMP #1. The range of the C_C for k_E compensation is 0 to 20 fF and should be varying linearly with s_1. Therefore, the initial dimensions of the k_E compensation metallizations can be determined from (4) and (5) as S_{fx} = 0.1 mm and S_{fy} = 0.3 mm. The dimensions finalized through EM simulations is provided in Fig. 6(a).

Maintaining 7% FBW across the frequency tuning range

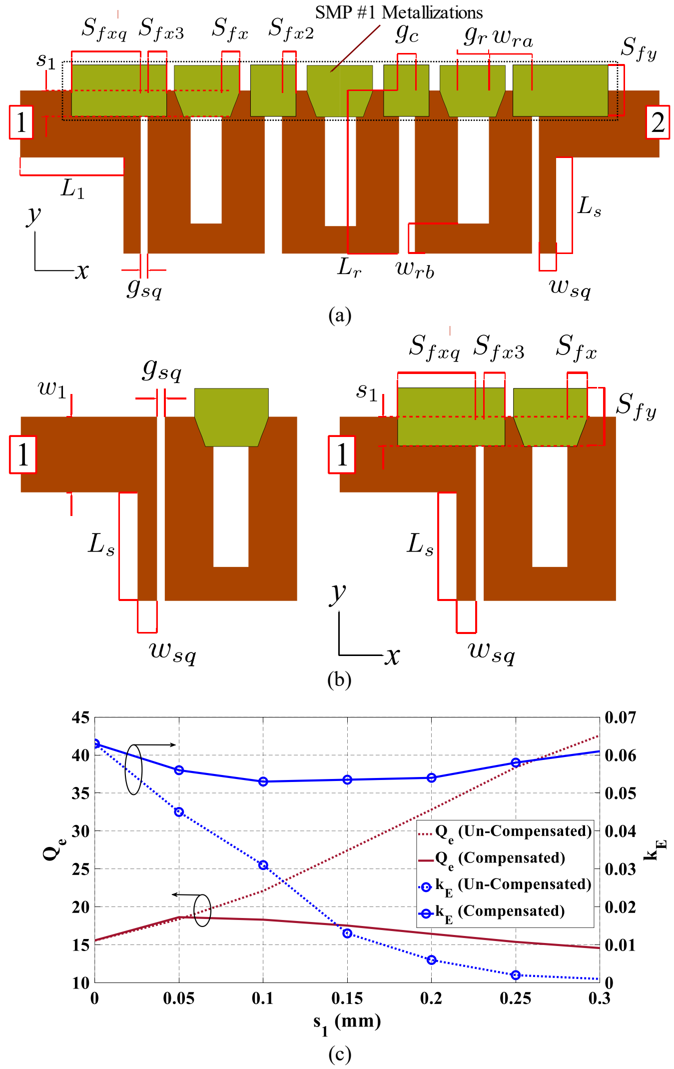

Fig. 6. (a) Layout for the FT-BPF filter with 7% constant FBW; (b) Q_e compensation scheme; (c) Q_e and k_E with and without SMP #1 coupling compensation metallizations. (L_1 = 0.6, w_1 = 0.39, L_r = 0.95, w_{ra} = 0.25, w_{rb} = 0.16, g_r = 0.18, g_c = 0.1, S_{fx} = 0.105, S_{fy} = 0.3, L_{fx} = 0.055, L_{fy} = 0.15, L_s = 0.56, w_{sq} = 0.1, g_{sq} = 0.04, S_{fxq} = 0.4, S_{fx2} = 0.08, S_{fx3} = 0.11, $0 \leq s_1 \leq S_{fy}$; dimensions are in mm).

requires to stabilize the Q_e variation as well. The filter is fed with a capacitively coupled microstrip line that is terminated in a shunt open-circuited stub. The stub serves two purposes: (i) stabilize the Q_e for lower frequencies similarly as in [3]; and (ii) provide a point where additional capacitive coupling can realized between the input/output line and the resonator through the SMP #2 metallizations (see Section IV for bandwidth tuning and Q_e variation discussion). The stub dimensions L_s and w_{sq} are designed to provide a stable Q_e as s_1 increases. Without any SMP #1 metallization loading, Q_e increases with the lowering of the resonance frequency due to the reduction in coupling between the input/output line and the resonator. Therefore, additional metallization traces are added into the SMP #1 to gradually compensate for the reduced coupling at the input ports of the filter. The detailed layout of the input side of the filter is provided in Fig. 6(b). For stabilizing Q_e, S_{fqx} = 0.4 mm is selected to maximize the capacitance between SMP #1 trace and input feed line. This allows to use smallest possible overlap

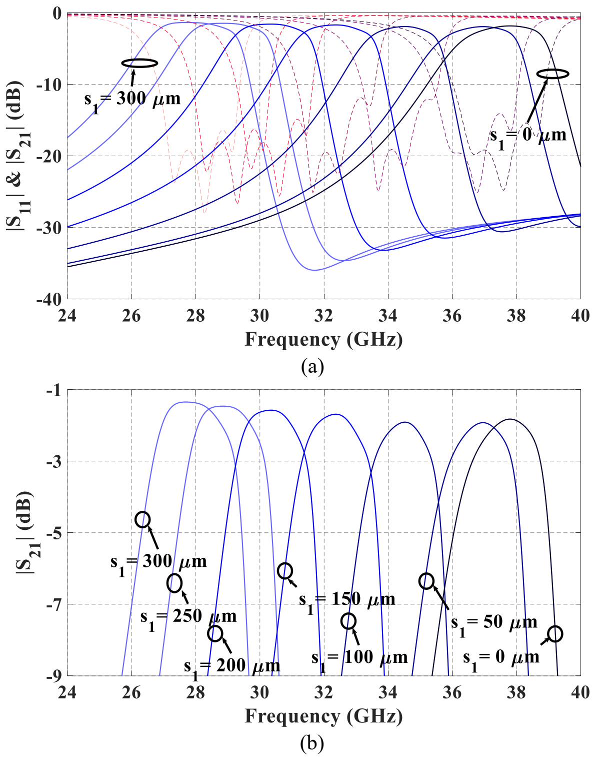

Fig. 7. Simulated performance of the FT-BPF: (a) $|S_{21}|$ and $|S_{11}|$; (b) close-up view of $|S_{21}|$ as a function of SMP #1 position s_1.

length S_{fx3}. Through EM simulations, S_{fx3} is found as 0.11 mm.

Fig. 6(c) demonstrates the effectiveness of coupling compensation traces included in the SMP #1. Specifically, the variation of the Q_e is 16.6±2. Likewise, k_E is maintained within the 0.058±0.006 range. The simulated S-Parameters of the filter are shown in Fig. 7 for s_1 varying from 0 to 0.3 mm in 0.05 mm steps. The filter operates as desired with 28 GHz to 38 GHz frequency tunability. The FBW is 7.68±0.39%. The deviation from 7% is due to the slight variations in k_E and Q_e. The IL of the simulated filter is 1.37 dB at 28 GHz and 1.83 dB at 38 GHz.

IV. Bandwidth Tunable Filter Design

The design of the BT-BPF follows from the constant FBW FT-BPF presented in the previous section. The layout of the filter is shown in Fig. 8(a). SMP #1 is removed. Hence, the center frequency of the filter is 38 GHz. SMP #2 is included in the layout for bandwidth tunability. Two of the SMP #2 rectangular traces are responsible for tuning k_E. The size of these traces (i.e. S_{cx} and S_{cy}) are designed in Section II to provide FBW tuning from 7% to 12% at 28 GHz. At 38 GHz, these traces increase k_E from 0.062 to 0.12. Therefore, the FBW tunability extends to be from 7.6% to 17.6% when Q_e of the input/output resonators are properly adjusted.

To maintain impedance matching across different values of SMP #2 position s_2 (i.e. across different FBW values), a Q_e reduction scheme is introduced. Specifically, SMP #2 hosts metallized traces that overlap with the input/output microstrip lines/stubs and resonators to provide increased capacitance as s_2 is increased. The overlap area is defined with parameters

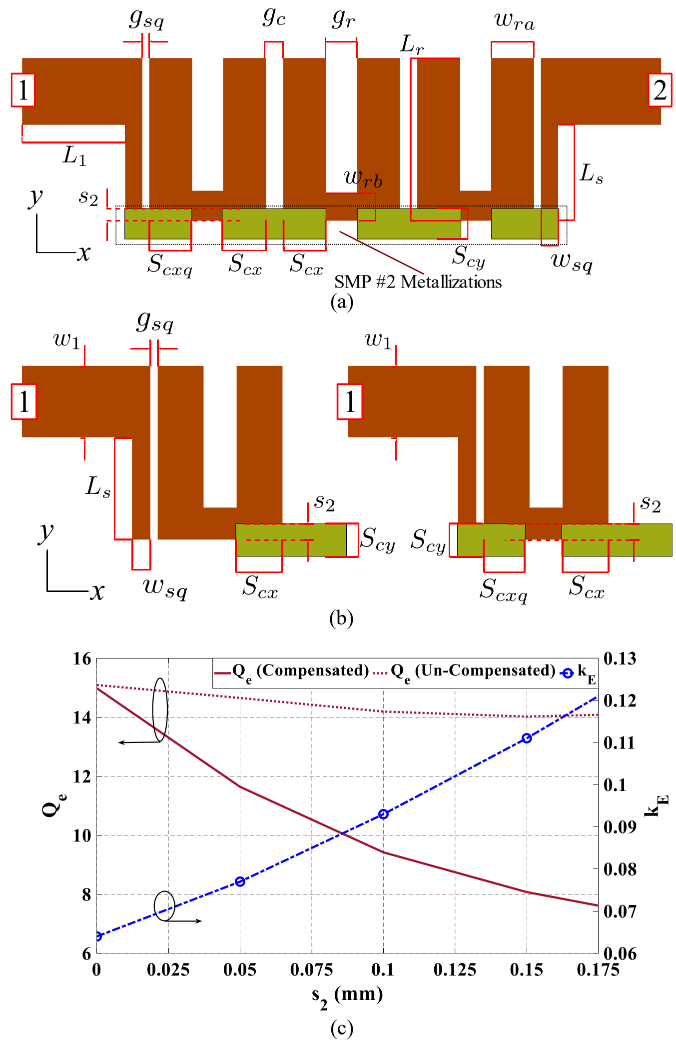

Fig. 8. (a) Layout of the BT-BPF; (b) Q_e compensation scheme; (c) Q_e and k_E with and without SMP #2 coupling compansation metallizations. ($L_1 = 0.6$, $w_1 = 0.39$, $L_r = 0.95$, $w_{ra} = 0.25$, $w_{rb} = 0.16$, $g_r = 0.18$, $g_c = 0.1$, $S_{cx} = 0.25$, $S_{cy} = 0.175$, $L_s = 0.56$, $w_{sq} = 0.1$, $g_{sq} = 0.04$, $S_{cxq} = 0.25$, $0 \le s_2 \le S_{cy}$; dimensions are in mm).

w_{sq}, S_{cxq}, and s_2. w_{sq} is set with the design of the coupling stub placed at the input/output microstrip lines. S_{cxq} is designed through simulations to provide the required Q_e reduction from 14.74 to 8.6 as k_E and FBW is increased. The layouts used for Q_e extraction and reduction are presented in Fig. 8(b). Designed Q_e and k_E variation with respect to SMP #2 position s_2 is shown in Fig. 8(c). Simulated S-parameters of the filter are presented in Fig. 9. It is observed that FBW can be tuned from 7.6% up to 17.6%. The filter performs with 1.8 dB and 0.95 dB IL in its 7.6% and 17.6% FBW states, respectively.

V. Frequency & Bandwidth Tunable Filter

The FBT-BPF can be designed as the combination of the FT-BPF and BT-BPF presented in above sections. Since FBT-BPF is loaded with both SMP #1 and SMP #2, two distinct microfluidic channels are needed. Consequently, the microfluidic channels are meandered as illustrated in Fig. 2. The microfluidic channel dimensions used for prototyping are provided in Section VII. Fig. 10(a) presents the layout. The simulated performance is shown in Fig. 10(b) for sampled filter

This is the author's version of an article that has been published in this journal. Changes were made to this version by the publisher prior to publication.
The final version of the record is available with Digital Object Identifier 10.1109/TMTT.2020.3006869

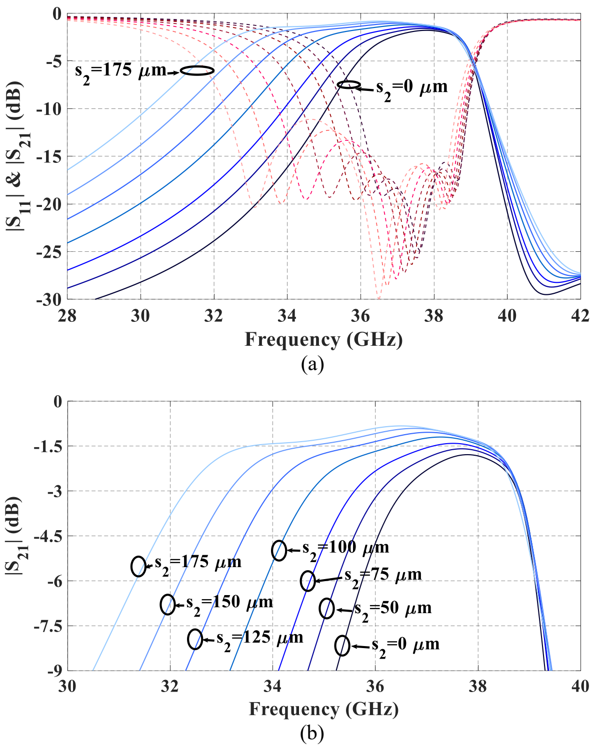

Fig. 9. Simulated performance of the BT-BPF: (a) $|S_{21}|$ and $|S_{11}|$; (b) close-up view of $|S_{21}|$ as a function of SMP #2 position s_2.

states. The maximum bandwidth is 17.6% and 12.5% at the highest (i.e. $s_1 = 0$ mm) and lowest resonance frequencies (i.e. $s_1 = 0.3$ mm), respectively. The frequency of operation can be tuned from 38 GHz down to 28 GHz with near constant FBW of 7.68 ± 0.39% for $s_2 = 0$. The IL performance of the filter is presented in Fig. 10(c). IL is less than 1.8 dB for all states. The worst-case IL is observed for the lowest FBW at highest operation frequency.

VI. Fabrication

Filter prototypes are fabricated with the substrate stack-ups shown in Fig. 1(a) and Fig. 5. The resonators and SMPs are realized with standard photolithography. All dimensions of the resonators, microstrip lines, coupling stubs, and SMP metallizations are oversized by 10 µm in mask generation to account for wet etching related undercut. The substrate of the resonators is bonded with a double-side copper-cladded 0.762 mm thick FR4 substrate using silver epoxy and a bonding press in order to provide mechanical rigidity. This completes the PCB preparation for the resonators. The SMPs are cut with a dicing saw from their main substrate. The metallization surfaces of the SMPs are deposited with 5 µm thick Parylene N by using a PDS 2010 Parylene Deposition System. Microfluidic channel walls with 360±10 µm height are fabricated on top of the PCB. These walls are formed by spin-coating the PCB with SU8 photoresist ($\varepsilon_r = 3.25$, $\tan\delta = 0.017$) and applying standard photolithography for patterning. The processing of the walls is done in two-steps of spin-coating by following the procedures described in [24, 25] for optimal exposure and baking times. The holes needed for channel inlets and outlets are drilled along with the holes needed for mounting the edge connectors. The SMPs are placed within the microfluidic channel walls. Sealing

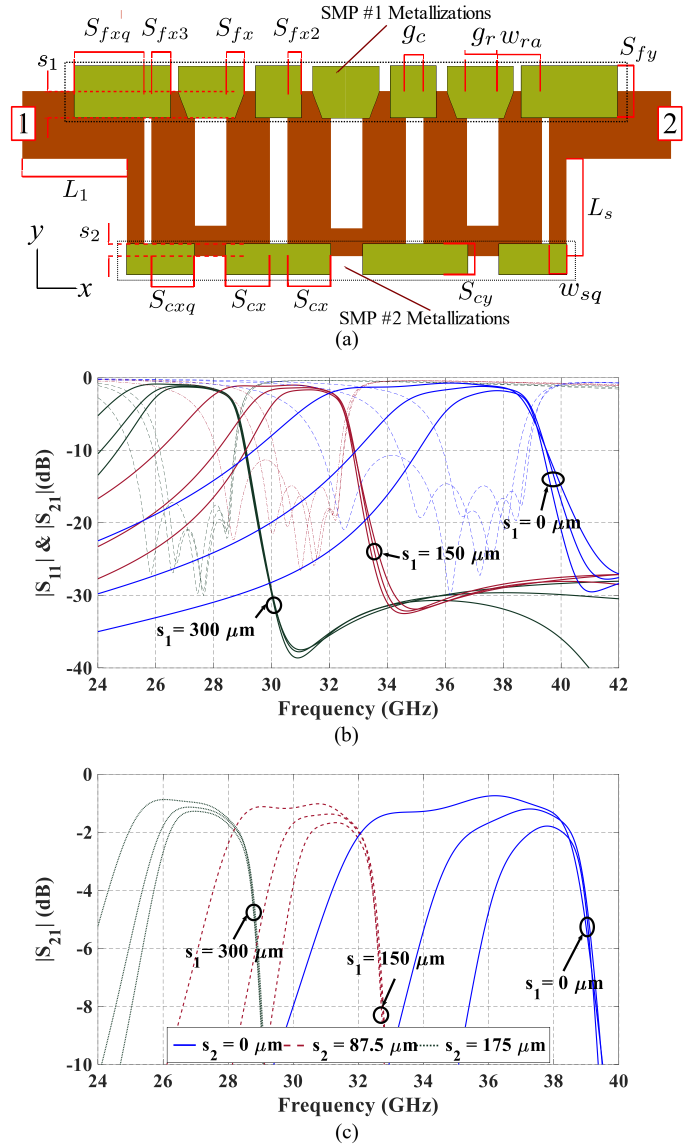

Fig. 10. (a) Layout of the FBT-BPF; (b) Simulated $|S_{21}|$, $|S_{11}|$, and (c) close-up view of $|S_{21}|$ as a function of SMP #2 position s_2. ($L_1 = 0.6$, $w_1 = 0.39$, $L_r = 0.95$, $w_{ra} = 0.25$, $w_{rb} = 0.16$, $g_r = 0.18$, $g_c = 0.1$, $S_{fx} = 0.105$, $S_{fy} = 0.3$, $L_{fx} = 0.055$, $L_{fy} = 0.15$, $S_{cx} = 0.25$, $S_{cy} = 0.175$, $L_s = 0.56$, $w_{sq} = 0.1$, $g_{sq} = 0.04$, $S_{fxq} = 0.4$, $S_{fx2} = 0.08$, $S_{fx3} = 0.11$, $S_{cxq} = 0.25$, $0 \le s_1 \le S_{fy}$, $0 \le s_2 \le S_{cy}$; dimensions are in mm).

the microfluidic channel with fused silica layer is carried out with the tenting technique [25]. Specifically, a ~50 µm thick film of soft-baked SU8 resist is placed on top of the channel walls to form the tented structure. Fused silica slide is coated with ~50 µm layer of SU8 photoresist for adhesive bonding. PCB and the dry film are heated to 48 °C and brought in contact with the coated fused silica slide to complete the sealing. 48 °C is below the glass transition of SU-8. It ensures that the dry film does not melt and flow inside the channel [26]. Following this process, the PCB is exposed and hard baked to complete the microfluidic channel sealing process.

The microfluidic channel reservoirs that will be placed under the bottom side of the PCB are fabricated with PDMS using soft-photolithography processes [26]. The thickness of the PDMS used for the microfluidic reservoirs are 3 mm. A 1 mm diameter punch is used to realize the channel filling ports in the PDMS substrate that will enable fitting of flexible hoses for introducing the FC-40 liquid into the microfluidic channel. Bonding of the PDMS with the copper layer at the bottom surface of the PCB is carried out with O_2 plasma (50 W, 30 s) treatment of the PDMS and APTES treatment of the copper layer. The copper layer is submerged in a 5% APTES solution for 20 minutes at 70 °C and dried out with a nitrogen gun before brought in contact with the plasma treated PDMS to form the irreversible bond [27]. In order to place the piezoelectric actuators on top of the PDMS based microfluidic channel reservoirs, the reservoir areas are first bonded with 25 µm thick LCP (Rogers ULTRALAM® 3850 with 9 µm copper cladding on both sides) following the APTES process described above. The piezoelectric actuators are bonded to the LCP layers using silver epoxy (EPO-TEK® H20E). This completes the fabrication process. As a final step, the microfluidic channels are filled with the FC-40 dielectric liquid. For this, flexible hoses are fit into the channel reservoirs, and the FC-40 liquid is introduced into the microfluidic channel with syringes connected to one-way stopcock valves with Luer connections (Cole-Parmer). After filling the channels, the valves are closed and Luer sealing plugs are connected to finalize closing the fluidic system. Prototypes maintain the valves and the plugs in case emptying/refilling of the microfluidic channels are needed. These components could be removed for stand-alone operation.

VII. Experimental Verification

FT-BPF and BT-BPF prototypes are shown in Fig. 11. These filters are fabricated with a single microfluidic channel that contain either the SMP #1 or SMP #2. Fig. 11(a) presents top and bottom views of the FT-BPF. The channel, SMP, and SMP metallization sizes are shown in Fig. 11 (b)-(e). The measured performance of the FT-BPF is shown in Fig. 12(a). It is found that SMP #1 completes its motion range with piezoelectric actuation voltage varying from 0 V to 129 V. The center frequency of the prototype is shifted to 41 GHz for the unloaded case (i.e. $s_1 = 0$ mm). This ~8% resonance frequency shift is due to the substrate stack-up used in Keysight ADS (see Fig. 5). The substrate stack-up maintains a uniform RO4003C substrate inside the microfluidic channel. However, the channel is partially filled with this substrate due to the physical size of the SMP. In the unloaded case, the SMP is completely removed, leaving the channel completely filled with the FC-40 dielectric liquid over the resonators. In addition, the channel walls partially overlap with resonators and this contributes to frequency and IL variation with respect to the simulations. Modeling non-uniform 2D substrate-stack-up and substrate stack-up variation as a function of SMP position requires employment of full-wave 3D EM simulators. However, due to the significant simulation times needed by 3D EM simulators, the filter designs presented have been carried out with Keysight ADS Momentum suite under a fixed substrate stack-up configuration. Simulating the unloaded filter layout in Keysight ADS with a 315 µm thick FC-40 liquid layer that replaces the RO4003C layer in the substrate stack-up shows a resonance frequency shift up to 42 GHz. Modeling the unloaded filter in 3D EM simulator Ansys HFSS v19.2 shows the resonance frequency at 41 GHz. These simulations verify the reasoning behind the 8% resonance frequency shift observed in experiments. The filter is found to be tunable from 28 GHz to

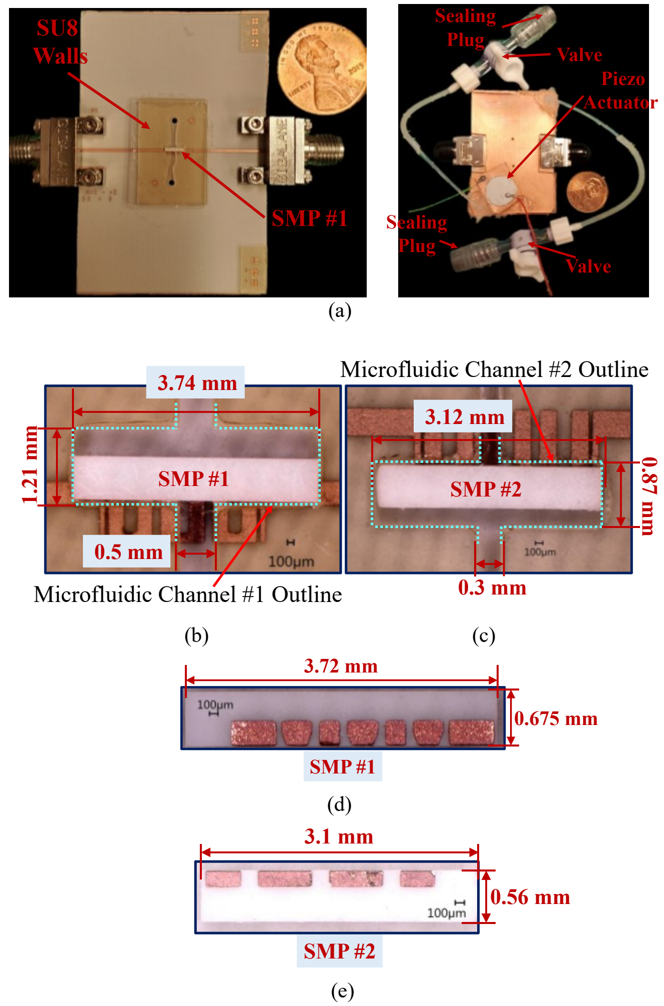

Fig. 11. (a) Top-side (left) and bottom-side views (right) of the FT-BPF prototype; (b) Microfluidic channel details of the FT-BPF; (c) Microfluidic channel details of BT-FPF; (d) SMP #1 of FT-BPF; (e) SMP #2 of BT-BPF.

41 GHz with SMP #1 position varied from $s_1 = 0$ mm to $s_1 = 0.3$ mm. The lower end of the frequency band is unchanged because the substrate-stack-up chosen in the Keysight ADS model is most accurate for the maximally loaded case of the resonators.

The measured IL of the filter is 3 dB and 4 dB at 38 GHz and 28 GHz, respectively. IL is better than 3 dB in majority of the frequency tuning range (i.e. 31 GHz – 41 GHz). The data represents ~1.2 dB increase in IL with respect to the simulations. This is mostly related to the half of the resonators being covered with lossy SU8 side walls. 3D EM simulator Ansys HFSS v19.2 determines IL as 3 dB for the unloaded case and fits with measurements. Fig. 12(b) presents the measured performance within 24 GHz – 64 GHz band. Out of band rejection of the filter is better than 25 dB for majority of the states. Second harmonic of the resonators are contributing to the degradation in the out of band rejection. Improvement may be possible by carrying out the design on thinner substrates and considering alternative resonators arrangements/types. Fig. 12(c) presents the close-up view of the IL when SMP #1 is actuated with voltages ranging from 0 V to 129 V. The filter maintains 7.8% ± 0.75% FBW. This is in very good agreement with the simulated performance.

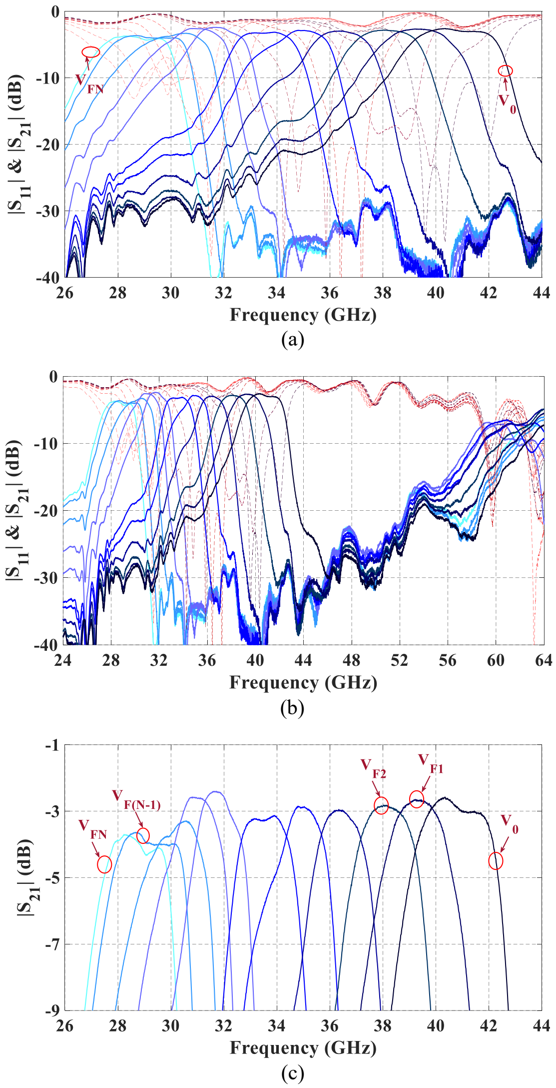

Fig. 12. Measured performance of the FT-BPF prototype for actuation voltages V_{FN}: (a) 26 GHz – 44 GHz response; (b) 24 GHz – 64 GHz response; (c) Close-up S_{21} response (V_{F0} = 0, V_{F1} = 56, V_{F2} = 66, V_{F3} = 70, V_{F4} = 77, V_{F5} = 86, V_{F6} = 95, V_{F7} = 105, V_{F8} = 114, V_{F9} = 124, and V_{F10} = 129 V).

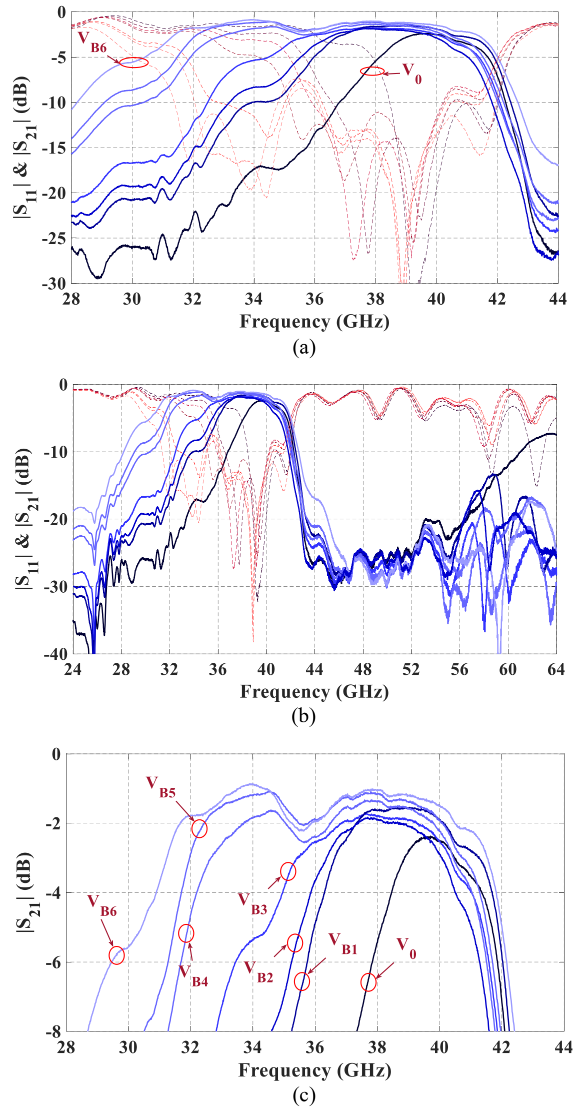

Fig. 13. Measured performance of the BT-BPF prototype for actuation voltages V_{BN}: (a) 28 GHz – 44 GHz response; (b) 24 GHz – 64 GHz response; (c) Close-up S_{21} response (V_0 = 0, V_{B1} = 54, V_{B2} = 78, V_{B3} = 88, V_{B4} = 96, V_{B5} = 104, V_{B6} = 115 V).

The measured performance of the BT-BPF is shown in Fig. 13(a) and (b). It is found that SMP #2 completes its motion range with piezoelectric actuation voltage varying from 0 V to 115 V. Fig. 13(c) presents the close-up view of the IL for different actuation voltages. SMP #2 can tune the filter bandwidth from 7.8% up to 16.7%. This is in good agreement with simulations. The filter performs with 2.6 dB IL at the lowest bandwidth and 1.9 dB IL at the highest bandwidth. The increase in IL and introduction of 1 dB ripple within the passband is associated with the differences in simulation-based substrate stack-up and the actual fabricated devices. These differences have been already explained for the FT-BPF.

The prototype of the FBT-BPF is shown in Fig. 14(a). A detailed view of the microfluidic channel dimensions is given in Fig 14(b). The measured S-parameter performance is shown in Fig. 15 (a)-(d). The bandwidth can be reconfigured from 7.8% to 16.7% at 38 GHz. Worst-case IL is 3.1 dB at 38 GHz and 1.95 dB at 28 GHz. The measured IL performance matches much better with the Keysight ADS simulated IL performance due to the minimized SU8 channel walls on the filter resonators to host two distinct SMPs. SMP #1 and SMP #2 complete their full motion ranges with piezoelectric actuation voltages varying within 0 V – 142 V and 0 V – 127 V, respectively. It is noticed that the actuation voltages are slightly increased in this filter with respect to the FT-BPF and BT-BPF. This can be attributed to the shape of the microfluidic channels used within this design. Meandering the microfluidic channels within the available circuit area has a consequence of employing narrower channel widths. This necessitates a larger fluidic pressure for mobilizing the SMPs [28], resulting in higher actuation voltages.

VIII. Reliability and Power Handling Characterization

The prototypes are tested for their reconfiguration speed, reliability, and power handling capability. In these tests, 1.85 mm end launch connectors were replaced with 2.92 mm end launch connectors. Therefore, this section shows the measured

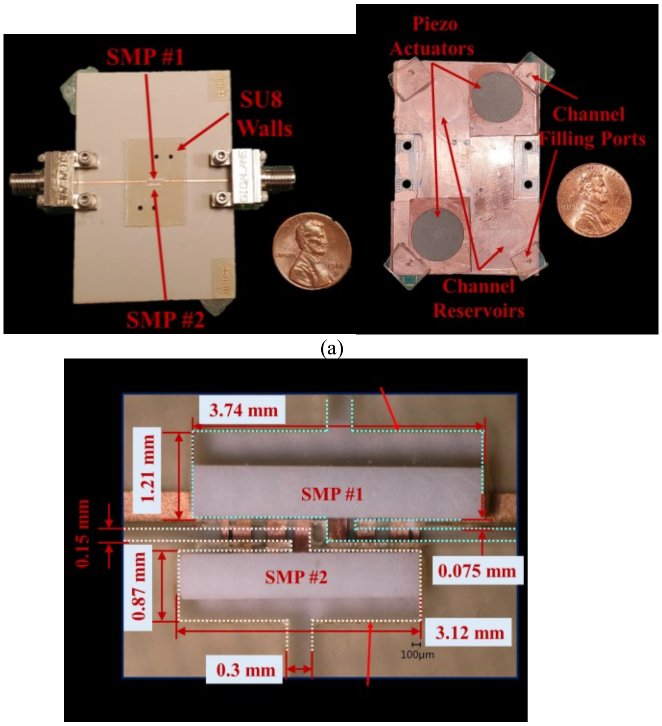

Fig. 14. (a) Prototype of the FBT-BPF; (b) Microfluidic channel details.

data up to 40 GHz. Reconfiguration speed is measured by using the set-up described in [11]. For this measurement, the FT-BPF is used. The filter is excited with continuous single tone RF signal at 28 GHz. SMP is actuated with a 50% duty cycle rectangular waveform (0 V to 127 V) while tracking the output of a mm-wave power detector diode (Krytar 203AK) connected to the output of the filter. Fig. 16 presents the detected voltage from the power detector. With the given setup, the signal received at the detector input was measured and set as -10 dBm at 28 GHz. This translates into ~46.4 mV received voltage at the detector output. At -25 dBm, the detected voltage measured is ~5 mV. With this information, reconfiguration speed can be estimated after the center frequency of the filter has shifted up enough to provide 15 dB attenuation at 28 GHz. This condition occurs after approximately 22.8 ms where the filter is estimated to have shifted ~6.5 GHz from its center frequency. Thus, reconfiguration speed for the filter is calculated as 285 MHz/ms. Additionally, the entire SMP actuation is expected to be within 35.8 ms.

For reliability testing, both FT-BPF and BT-BPF prototypes are actuated with a 20 Hz 50 % duty cycle rectangular waveform (0 V to 127 V) for 7 days. S-parameters of the filters are measured approximately after they are actuated 100×10^3, 1×10^6, 5×10^6 and 12×10^6 times. Fig. 17 and Fig. 18 show the measured performance for the FT-BPF and BT-FPF, respectively. For simplicity, the measured response is only shown at 3 possible actuation voltages. It is observed that filters operate without major degradation in IL performance. For a given actuation voltage, center frequency shows variations less than 1%. This is likely due to the mechanical nature of the reconfiguration scheme used and possible uncertainties of SMP position as the plate moves suspended in dielectric liquid. The repeatability test is stopped at ~12,000,000 cycles due to the

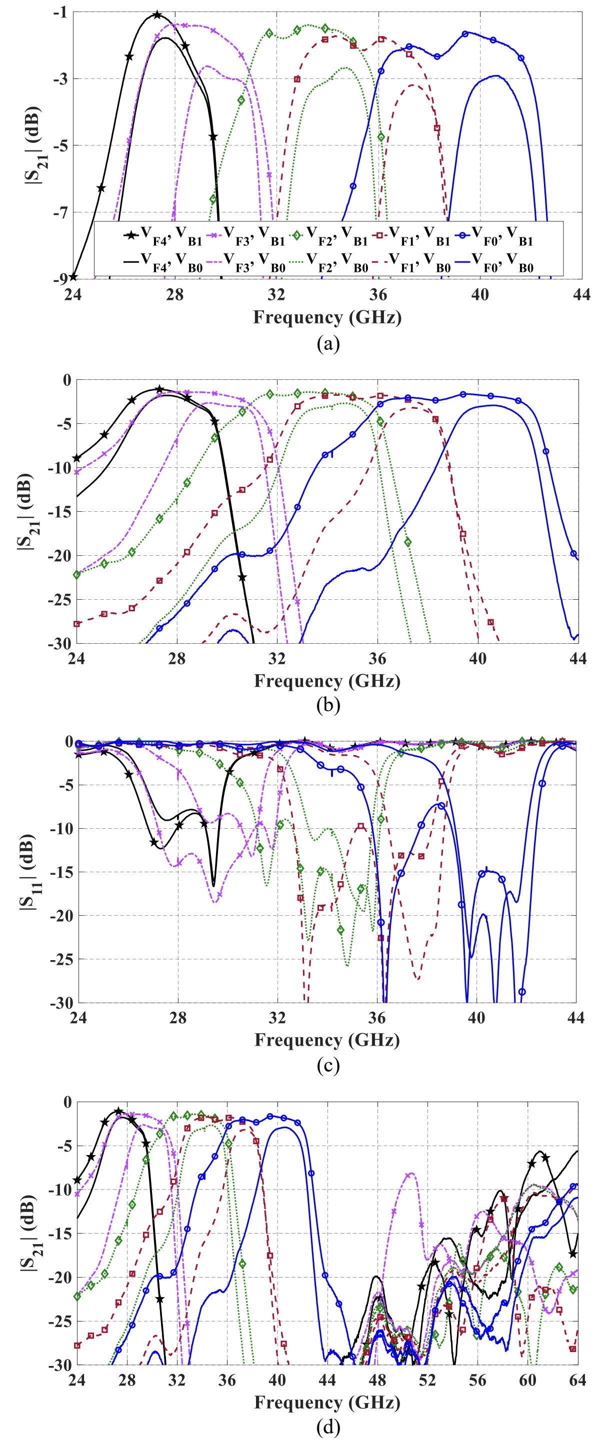

Fig. 15. Measured performance of the FBT-BPF prototype for actuation voltages V_{FN} and V_{BM}: (a) 24 GHz – 44 GHz S_{21} response; (b) 24 GHz – 44 GHz S_{11} response; (c) 24 GHz – 64 GHz S_{21} response ($V_{F0} = 0$ V, $V_{F1} = 64$ V, $V_{F2} = 87$ V, $V_{F3} = 125$ V, $V_{F4} = 142$ V, $V_{B0} = 0$ V, $V_{B1} = 127$ V).

frequency tunable filter developing a leak at the bonding interface between the fused silica and the SU8 channel walls. More investigations and repeatability testing are needed to fully understand if this is an isolated case associated with bonding parameters.

The FBT-BPF prototype is used for power handling characterization. This is motivated from the fact that this filter operates with the lowest measured IL. The experiment setup is

TABLE I
PERFORMANCE COMPARISON WITH STATE OF THE ART FILTERS

Reference	Technology	Frequency Range (GHz)	IL (dB)	Tuning Type	FBW (%)		Tuning Ratio	Continuous Power (W)	Reconfiguration Speed
					Constant	Tunable			
[29]	Microstrip (Varactor)	0.7–1.1	7–1.5	Continuous (Freq. Only)	-	7–27	1.6:1	0.32	-
[30]	Microstrip (PIN Diode)	20.5–21.3	9–8	Discrete (Freq. Only)	4.2±0.6	No	1.04:1	-	-
[31]	MEMS	18.6–21.4	4.2–3.9	Discrete (Freq. Only)	7.5±0.1	No	1.15:1	-	-
[32]	EVA (MEMS)	20–40	2.9	Continuous (Freq. Only)	3.3±1.4	No	2:1	-	10–60 µs*
[33]	SIW	20–26.5	3.2–3.4	Continuous (Freq. Only)	3±0.2	No	1.33:1	-	-
[34]	BST	28–34	3.8–2.8	Continuous (Freq. Only)	12.1±1.1	No	1.21:1	-	-
[35]	Microfluidics (CPW)	3.4–5.5	2.35–4.8	Discrete (Freq. Only)	5±0.35	No	1.6:1	10	-
[36]	Microfluidics (Microstrip)	3.75–4.75	0.6	Discrete (Freq. Only)	39±2.5	No	1.19:1	-	70±20 ms
[3]	Microfluidics (Microstrip)	1.5–4.0	2.5–4	Continuous (Freq. Only)	5	No	2.7:1	15	2.5 MHz/ms
This Work	Microfluidics (Microstrip)	28–41	1.9–3.1	Continuous (Freq. and FBW)	7.8±0.75	7.8–16.7	1.46:1	5	285 MHz/ms

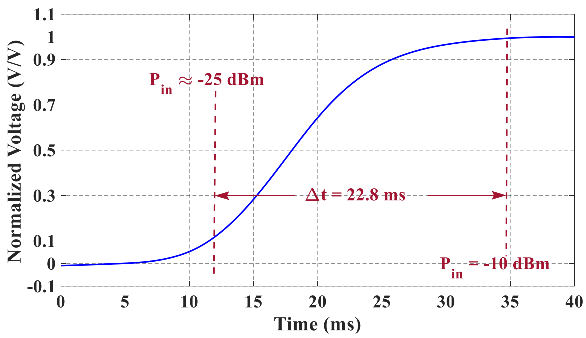

Fig. 16. Measured reconfiguration time for the FT-BPF prototype.

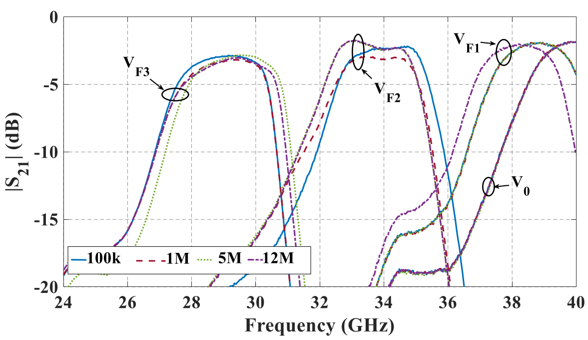

Fig. 17. FT-BPF prototype performance. S_{21} performance after different actuation cycles ($V_0 = 0$ V, $V_{F1} = 56$ V, $V_{F2} = 86$ V, $V_{F3} = 129$ V).

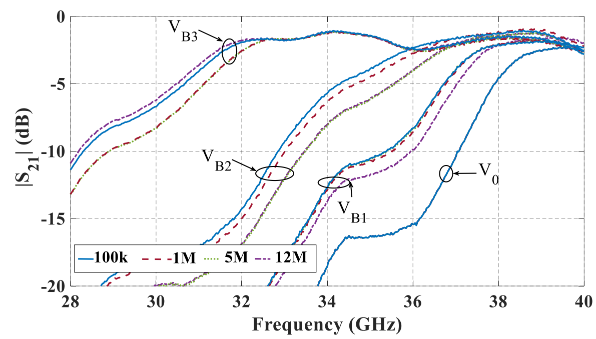

Fig. 18. BT-BPF prototype performance. S_{21} performance after different actuation cycles ($V_0 = 0$ V, $V_{B1} = 54$ V, $V_{B2} = 88$ V, $V_{B3} = 115$ V).

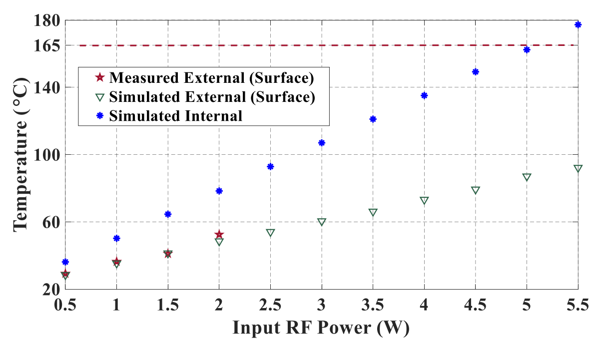

Fig. 19. Measured temperatures at different input RF powers for the combined frequency and bandwidth reconfigurable filter prototype.

similar to the one described in [14]. The filter is excited with continuous RF power at 38 GHz. The actuation condition selected for the power characterization is when the SMP #2 does not load the filter (i.e. smallest possible FBW). SMP #1 is actuated to shift center frequency of the filter to 38 GHz. These actuation voltage settings make the dual-tunable filter operate at its highest IL state to maximize the RF power dissipation. The filter is excited with RF power varying from 0.5 W to 2 W. Temperature measurements are taken after a steady-state condition is achieved for the given input power by using a thermal camera (Keysight U5850 TrueIR). Multiphysics simulations are performed with Ansys 19.2 Workbench to verify the experiments. Measured temperatures at filter surface and simulated temperatures agree quite well as shown in Fig. 19. Simulations indicate that at 5 W of input RF power the internal temperature of the device rises to 162 °C. This is slightly below the boiling temperature of FC-40 (i.e. 165 °C). Therefore, 5 W can be considered as the maximum continuous RF power handling level. Power handling can further be enhanced by resorting to thicker ground planes and/or heat sinks. Characterization of intermodulation components is not possible with our given measurement setup since we are limited to 2 W input RF power. Considering the use of microfluidic technology however, previous research groups have tried to perform such characterization and noted that high power levels (>65 dBm) are needed to measure IIP_3 products [35]. Table I presents a performance comparison of several state-of-the-art reconfigurable filters. IL performance of the microfluidic reconfiguration approach benefits from the lack of active components. Typical IL performance for implementations of reconfigurable filters with varactor/PIN diodes is in the order of >7 dB, which can be expected to further increase in the 38 GHz band. Similarly, power handling capabilities are expected to be higher for the microfluidic technology than for varactors. The expected DC power consumption for this device is about 18 mW and similar to the SPST switch introduced in [11]. One relevant point of interest to mention is the relative SMP sensitivity to vibrations, device tilt, or external pressure forces that might cause random and unwanted SMP motion. During measurements it was visually observed that external pressure applied with a finger on the flexible PDMS membrane, would in turn cause SMP motion. This is expected considering that the piezo actuator functions with the same principle. This implies that design considerations need to be made to avoid unwanted forces from activating the membrane. Regarding tilt however, device performance remained unchanged as some limited tests were performed with the filters on vertical and upside-down positions. Further testing is planned to accurately characterize these phenomena and their effect on device performance, specifically, long-term vibration table tests are expected to offer more insight on these effects.

IX. Concluding Remarks

The design, implementation, and characterization of a microfluidically reconfigurable coupled resonator filter with integrated actuation was presented for the first time. Three filters were considered to demonstrate the capabilities of microfluidic actuation at mm-wave frequencies. Specifically, a constant FBW FT-BPF, a BT-BPF, and an FBT-BPF were demonstrated. It was shown that the frequency and bandwidth tunable filter performs with worst-case 3.1 dB IL, while exhibiting a constant 7.8% ± 0.75% FBW and bandwidth tunability within 7.8% to 16.7%. Although third order filters were demonstrated, the concepts demonstrated in this paper can be extended for higher order filters. Integrated actuation mechanism allowed for long-term repeatability tests of microfluidically reconfigurable RF devices for the first time. It was demonstrated that the filter performs with no major degradation in IL performance and can be reconfigured at 285 MHz/ms, implying about 35.8 ms reconfiguration for the whole frequency range of 28 GHz – 41 GHz. Power handling characterization shows that the filter could handle up to 5 W of continuous RF power without the need of a thick ground plane or external cooling. The filters were continuously actuated up to 12 M cycles during 7 days of testing. It is possible that the device life can be much larger than 12 million cycles and further investigations are necessary. In addition, further investigations could lead to optimization of reconfiguration speeds by employing different channel shapes, fabrication techniques, and miniaturized plate sizes. Similarly, required actuation voltages can be potentially reduced by these optimizations or with the inclusion of a second piezo actuator at the secondary reservoir location. Finally, with the presented device performance these types of devices could be readily deployed for mm-wave applications within the 28 GH to 38 GHz bands since they meet the current bandwidth requirements. These filters could be employed in any any component that can benefit from the low-cost, ease of manufacturing, and high-power/high-efficiency capabilities of microfluidic reconfiguration.

X. References

[1] G. Mumcu, "Microfluidically reconfigurable antennas," in *Electromagnetic Waves*, *Developments in Antenna Analysis and Design: Volume 1*: Institution of Engineering and Technology, 2018, pp. 203-241.

[2] K. Entesari and A. P. Saghati, "Fluidics in Microwave Components," *IEEE Microwave Magazine,* vol. 17, no. 6, pp. 50-75, Jun 2016, DOI: 10.1109/Mmm.2016.2538513.

[3] T. Palomo and G. Mumcu, "Microfluidically Reconfigurable Microstrip Line Combline Filters With Wide Frequency Tuning Capabilities," *IEEE Transactions on Microwave Theory and Techniques,* http://doi.org/10.1109/TMTT.2017.2730181 vol. 65, no. 10, pp. 3561-3568, 2017.

[4] A. Dey and G. Mumcu, "Microfluidically Controlled Frequency-Tunable Monopole Antenna for High-Power Applications," *IEEE Antennas and Wireless Propagation Letters,* vol. 15, pp. 226-229, 2016, DOI: 10.1109/Lawp.2015.2438863.

[5] A. P. Saghati, J. S. Batra, J. Kameoka, and K. Entesari, "Miniature and Reconfigurable CPW Folded Slot Antennas Employing Liquid-Metal Capacitive Loading," *IEEE Transactions on Antennas and Propagation,* vol. 63, no. 9, pp. 3798-3807, Sep 2015, DOI: 10.1109/Tap.2015.2447002.

[6] A. A. Gheethan, A. Dey, and G. Mumcu, "Passive Feed Network Designs for Microfluidic Beam-Scanning Focal Plane Arrays and Their Performance Evaluation," *IEEE Transactions on Antennas and Propagation,* vol. 63, no. 8, pp. 3452-3464, Aug 2015, DOI: 10.1109/Tap.2015.2436441.

[7] E. Gonzalez and G. Mumcu, "Low-Loss Wideband Feed Networks for High Gain Microfluidic Beam-Scanning Focal Plane Arrays," *2016 IEEE Antennas and Propagation Society International Symposium,* pp. 645-646, 2016.

[8] Q. Q. Liu and N. C. Tien, "Design and Modeling of Liquid Gallium Contact Rf Mems Switch," *Proceedings of the Asme Micro/Nanoscale Heat and Mass Transfer International Conference, Vol 3,* pp. 191-198, 2010.

[9] P. Sen and C. J. Kim, "A Liquid-Solid Direct Contact Low-Loss RF Micro Switch," *Journal of Microelectromechanical Systems,* vol. 18, no. 5, pp. 990-997, Oct 2009, DOI: 10.1109/Jmems.2009.2029170.

[10] S. Khan, N. Vahabisani, and M. Daneshmand, "A Fully 3-D Printed Waveguide and Its Application as Microfluidically Controlled Waveguide Switch," *IEEE Transactions on Components Packaging and Manufacturing Technology,* vol. 7, no. 1, pp. 70-80, Jan 2017, DOI: 10.1109/Tcpmt.2016.2631545.

[11] E. González and G. Mumcu, "Integrated Actuation of Microfluidically Reconfigurable mm-Wave SPST Switches," *IEEE Microwave and Wireless Components Letters,* vol. 29, no. 8, pp. 541-544, 2019, DOI: 10.1109/LMWC.2019.2925889.

[12] T. Palomo and G. Mumcu, "Highly Reconfigurable Bandpass Filters Using Microfluidically Controlled Metallized Glass Plates," *2014 IEEE MTT-S International Microwave Symposium (IMS),* 2014.

[13] E. González and G. Mumcu, "Mm-Wave Beam-Steering Focal Plane Arrays with Microfluidically Switched Feed Networks," *IEEE Transactions on Antennas and Propagation,* pp. 7424 - 7429, 2018, DOI: 10.1109/TAP.2018.2874488.

[14] E. González and G. Mumcu, "Microfluidic Switches with Integrated Actuation for Mm-Wave Beam-Steering Arrays," in *2019 IEEE International Symposium on Antennas and Propagation and USNC-URSI Radio Science Meeting*, 7-12 July 2019 2019, pp. 1871-1872, DOI: 10.1109/APUSNCURSINRSM.2019.8889274.

[15] T. Palomo and G. Mumcu, "Microfluidically Reconfigurable Metallized Plate Loaded Frequency-Agile RF Bandpass Filters," *IEEE Transactions on Microwave Theory and Techniques,* http://doi.org/10.1109/TMTT.2015.2504473 vol. 64, no. 1, pp. 158-165, 2016.

[16] Federal Communcations Commission. "Radio Spectrum Allocation." https://www.fcc.gov/engineering-technology/policy-and-rules-division/general/radio-spectrum-allocation (accessed.
[17] GSM Association. "5G Spectrum Guide – Everything You Need to Know." https://www.gsma.com/spectrum/5g-spectrum-guide/
[18] J.-S. Hong and Wiley InterScience (Online service), *Microstrip filters for RF/microwave applications*, 2nd ed. Hoboken, N.J.: Wiley,, 2011, pp. 1 online resource (xvi, 635 p.). [Online]. Available: http://onlinelibrary.wiley.com/book/10.1002/9780470937297.
[19] M. Sanchez-Renedo, R. Gomez-Garcia, J. I. Alonso, and C. Briso-Rodriguez, "Tunable combline filter with continuous control of center frequency and bandwidth," *IEEE Transactions on Microwave Theory and Techniques,* vol. 53, no. 1, pp. 191-199, 2005, DOI: 10.1109/TMTT.2004.839309.
[20] T. Cheng and K. Tam, "A Wideband Bandpass Filter With Reconfigurable Bandwidth Based on Cross-Shaped Resonator," *IEEE Microwave and Wireless Components Letters,* vol. 27, no. 10, pp. 909-911, 2017, DOI: 10.1109/LMWC.2017.2746679.
[21] P. Jae-Hyoung, L. Sanghyo, K. Jung-Mu, K. Hong-Teuk, K. Youngwoo, and K. Yong-Kweon, "Reconfigurable millimeter-wave filters using CPW-based periodic structures with novel multiple-contact MEMS switches," *Journal of Microelectromechanical Systems,* vol. 14, no. 3, pp. 456-463, 2005, DOI: 10.1109/JMEMS.2005.844849.
[22] D. Yingjie, P. Gardner, P. S. Hall, H. Ghafouri-Shiraz, and Z. Jiafeng, "Multiple-coupled microstrip hairpin-resonator filter," *IEEE Microwave and Wireless Components Letters,* vol. 13, no. 12, pp. 532-534, 2003, DOI: 10.1109/LMWC.2003.819377.
[23] J.-S. G. Hong and M. J. Lancaster, *Microstrip filters for RF/microwave applications* (Wiley series in microwave and optical engineering). New York ; Chichester England: Wiley, 2001, pp. xii, 471 pages.
[24] T. A. Anhoj, A. M. Jorgensen, D. A. Zauner, and J. Hübner, "The effect of soft bake temperature on the polymerization of SU-8 photoresist," *Journal of Micromechanics and Microengineering,* vol. 16, no. 9, pp. 1819-1824, 2006/07/28 2006, DOI: 10.1088/0960-1317/16/9/009.
[25] M. Gaudet and S. Arscott, "A user-friendly guide to the optimum ultraviolet photolithographic exposure and greyscale dose of SU-8 photoresist on common MEMS, microsystems, and microelectronics coatings and materials," *Analytical Methods,* 10.1039/C7AY00564D vol. 9, no. 17, pp. 2495-2504, 2017, DOI: 10.1039/C7AY00564D.
[26] A. A. Gheethan, M. C. Jo, R. Guldiken, and G. Mumcu, "Microfluidic Based Ka-Band Beam-Scanning Focal Plane Array," *IEEE Antennas and Wireless Propagation Letters,* http://doi.org/10.1109/LAWP.2013.2294153 vol. 12, pp. 1638-1641, 2013.
[27] Y. K. H. Cho, Hyun Doo; Park, Dong Kyu; Vijaya Sunkara, "Method for bonding substrates ", Patent Appl. KR20120053029A·2012-05-18, 2012.
[28] M. Bahrami, M. M. Yovanovich, and J. R. Culham, "Pressure Drop of Fully-Developed, Laminar Flow in Microchannels of Arbitrary Cross-Section," *Journal of Fluids Engineering,* vol. 128, no. 5, pp. 1036-1044, 2006, DOI: 10.1115/1.2234786.
[29] C. Schuster *et al.*, "Performance Analysis of Reconfigurable Bandpass Filters With Continuously Tunable Center Frequency and Bandwidth," *IEEE Transactions on Microwave Theory and Techniques,* vol. 65, no. 11, pp. 4572-4583, 2017, DOI: 10.1109/TMTT.2017.2742479.
[30] B. Rohrdantz, V. Schmidt, and A. F. Jacob, "Microstrip ring resonator based frequency reconfigurable band-pass filters at K-band," in *2014 20th International Conference on Microwaves, Radar and Wireless Communications (MIKON)*, 16-18 June 2014 2014, pp. 1-4, DOI: 10.1109/MIKON.2014.6899907.
[31] A. Abbaspour-Tamijani, L. Dussopt, and G. M. Rebeiz, "Miniature and tunable filters using MEMS capacitors," *IEEE Transactions on Microwave Theory and Techniques,* vol. 51, no. 7, pp. 1878-1885, 2003, DOI: 10.1109/TMTT.2003.814317.
[32] Z. Yang, D. Psychogiou, and D. Peroulis, "Design and Optimization of Tunable Silicon-Integrated Evanescent-Mode Bandpass Filters," *IEEE Transactions on Microwave Theory and Techniques,* vol. 66, no. 4, pp. 1790-1803, 2018, DOI: 10.1109/TMTT.2018.2799575.
[33] P. Adhikari, W. Yang, and D. Peroulis, "A 20–26.5-GHz PCB Bandpass Filter Tuned With Contactless Tuners," *IEEE Microwave and Wireless Components Letters,* vol. 29, no. 8, pp. 513-515, 2019, DOI: 10.1109/LMWC.2019.2922496.
[34] K. Choi, S. Courreges, Z. Zhao, J. Papapolymerou, and A. Hunt, "X-band and Ka-band tunable devices using low-loss BST ferroelectric capacitors," in *2009 18th IEEE International Symposium on the Applications of Ferroelectrics*, 23-27 Aug. 2009 2009, pp. 1-6, DOI: 10.1109/ISAF.2009.5307566.
[35] A. P. Saghati, J. S. Batra, J. Kameoka, and K. Entesari, "A Miniaturized Microfluidically Reconfigurable Coplanar Waveguide Bandpass Filter With Maximum Power Handling of 10 Watts," *IEEE Transactions on Microwave Theory and Techniques,* vol. 63, no. 8, pp. 2515-2525, 2015, DOI: 10.1109/TMTT.2015.2446477.
[36] D. L. Diedhiou, R. Sauleau, and A. V. Boriskin, "Microfluidically Tunable Microstrip Filters," *IEEE Transactions on Microwave Theory and Techniques,* vol. 63, no. 7, pp. 2245-2252, 2015, DOI: 10.1109/TMTT.2015.2435704.